Uncertainties in Microwave Properties of Frozen Precipitation: Implications for Remote Sensing and Data Assimilation

MARK S. KULIE AND RALF BENNARTZ

Department of Atmospheric and Oceanic Science, University of Wisconsin—Madison, Madison, Wisconsin

THOMAS J. GREENWALD

Cooperative Institute for Meteorological Satellite Studies, University of Wisconsin—Madison, Madison, Wisconsin

YONG CHEN

Joint Center for Satellite Data Assimilation, Camp Springs, Maryland

FUZHONG WENG

NOAA/NESDIS/Office of Research and Applications, and Joint Center for Satellite Data Assimilation, Camp Springs, Maryland

(Manuscript received 5 April 2010, in final form 21 June 2010)

ABSTRACT

A combined active/passive modeling system that converts *CloudSat* observations to simulated microwave brightness temperatures (T_B) is used to assess different ice particle models under precipitating conditions. Simulation results indicate that certain ice models (e.g., low-density spheres) produce excessive scattering and implausibly low simulated T_Bs for stratiform precipitation events owing to excessive derived ice water paths (IWPs), while other ice models produce unphysical T_B depressions due to the combined effects of elevated derived IWP and excessive particle size distribution–averaged extinction. An ensemble of nonspherical ice particle models, however, consistently produces realistic results under most circumstances and adequately captures the radiative properties of frozen hydrometeors associated with precipitation—with the possible exception of very high IWP events. Large derived IWP uncertainties exceeding 60% are also noted and may indicate IWP retrieval accuracy deficiencies using high-frequency passive microwave observations. Simulated T_B uncertainties due to the ice particle model ensemble members approach 9 (5) K at 89 (157) GHz for high ice water path conditions associated with snowfall and ~2–3 (~1–2) K under typical stratiform rain conditions. These uncertainties, however, display considerable variability owing to ice water path, precipitation type, satellite zenith angle, and frequency. Comparisons between 157-GHz simulations and observations under precipitating conditions produce low biases (<1.5 K) and high correlations, but lower-frequency channels display consistent negative biases of 3–4 K in precipitating regions. Sample error correlations and covariance matrices for select microwave frequencies also show strong functional relationships with ice water path and variability depending on precipitation type.

1. Introduction

Satellite-based passive microwave instruments have provided routine retrievals of important geophysical parameters over the past few decades, while recent spaceborne active microwave instruments have generated valuable datasets of cloud and precipitation profiles. Cloud and precipitation research has particularly benefited from sustained microwave observations that have enabled the development and continual improvement of global cloud and precipitation climatologies (e.g., Weng et al. 1997; O'Dell et al. 2008; Hilburn and Wentz 2008; Liu and Zipser 2009; Ellis et al. 2009). These climatologies not only are useful to study the global distribution of clouds and precipitation, but also serve as valuable

Corresponding author address: Mark S. Kulie, Department of Atmospheric and Oceanic Sciences, University of Wisconsin—Madison, 1225 W. Dayton St., Madison, WI 53706.
E-mail: mskulie@wisc.edu

DOI: 10.1175/2010JAS3520.1

© 2010 American Meteorological Society

independent datasets to evaluate global climate and numerical weather prediction (NWP) models.

In addition to model validation, global microwave observations enhance operational NWP applications via data assimilation. This topic has received considerable attention in recent years owing to the valuable information content contained in microwave observations that increases forecast skill (e.g., English et al. 2000; Mahfouf et al. 2005; Weng et al. 2007; Kelly et al. 2008). Clear-sky data assimilation is a largely tractable problem, and clear-sky microwave observations have been routinely assimilated operationally in NWP models over the past two decades. Advances in all-weather microwave radiance assimilation have been aided by the recent development of computationally efficient and accurate radiative transfer (RT) models for scattering-intensive conditions commonly associated with clouds and precipitation (e.g., Greenwald et al. 2005; Heidinger et al. 2006; Liu and Weng 2006; Evans 2007). Assimilation of microwave radiances under cloudy and/or precipitating conditions, however, is still rife with complexities (see Errico et al. 2007a,b and references therein), and only recently have operational centers assimilated all-weather observations (Bauer et al. 2006a,b).

Properly characterizing forward modeling errors is essential for effectively incorporating microwave radiances under cloudy and precipitating conditions in operational data assimilation. Numerous possible forward modeling error sources (e.g., the RT solver, cloud microphysical assumptions, surface emissivity parameterizations, three-dimensional effects, and others) define the total observation/operator error and its related covariance matrix, which influence how the observations are utilized within the data assimilation procedure. To illustrate this issue, O'Dell et al. (2006) reported significant differences in error correlations and covariances due to the choice of RT model for select microwave frequencies. Granted, the model errors studied in O'Dell et al. (2006) are less important than some of the other possible forward model error sources previously listed, but they still displayed markedly different behavior depending on the RT solver. More work must be undertaken to study the larger sources of observation/operator error and their subsequent impact on data assimilation.

This study focuses on one such forward model error source related to cloud microphysics—modeling the scattering and extinction properties of frozen hydrometeors—that can produce significant model uncertainties. The scattering signature at higher microwave frequencies due to precipitation-sized frozen hydrometers has been well documented (e.g., Spencer et al. 1989; Petty 1994; Bennartz and Petty 2001) and serves as the primary physical basis for passive microwave remote sensing of precipitation, especially over land surfaces (e.g., Kongoli et al. 2003; McCollum and Ferraro 2003). Describing the complex interaction of microwave radiation with a diverse population of frozen particles is important for properly characterizing the scattering signal, and numerous studies have attempted to find both realistic and computationally inexpensive methods to perform this challenging task. Frozen hydrometeors have commonly been modeled as low-density spheres (e.g., Bauer et al. 1999; Bennartz and Petty 2001; Zhao and Weng 2002, among many others), and recent efforts have produced single-scattering properties for nonspherical habits suitable for microwave remote sensing (e.g., Hong 2007; Kim et al. 2007; Liu 2008; Petty and Huang 2010). Physically assessing these various ice particle models under precipitating conditions is a necessary and critical task for microwave precipitation retrieval development and data assimilation purposes.

In this study, a modeling system will be described allowing both active and passive microwave response to clouds and precipitation to be modeled in a framework requiring relevant backscatter and extinction properties of ice models to be physically consistent. This approach uses *CloudSat* data to provide vertical profiles of hydrometeors that are subsequently utilized to simulate multifrequency passive microwave brightness temperatures. The centerpiece of this combined active/passive modeling system is a database containing over 25 ice particle models and their associated physical properties that allows side-by-side objective assessment of these ice models over a wide microwave spectral range and enables realistic forward model uncertainties due to ice model properties to be established. Simulated brightness temperatures can also be compared with passive microwave observations to study model errors under all-weather conditions.

Sections 2 and 3 respectively describe the data sources employed in this study and a methodology overview of the active/passive modeling system. An assessment of ice particle models for a synoptic precipitation event is presented in section 4, and global comparison statistics and sample error correlations and covariances are shown in section 5. A summary and concluding remarks are provided in section 6.

2. Data

The data utilized in this study are from the following instruments: *CloudSat*'s Cloud Profiling Radar (CPR), the Advanced Microwave Scanning Radiometer for Earth Observing System (AMSR-E), and the Microwave Humidity Sounder (MHS).

CloudSat (Stephens et al. 2002) carries the single-frequency, W-band (94 GHz) CPR (Tanelli et al. 2008) and has provided cloud and precipitation profiles since

2006. The CPR is a nonscanning, near-nadir-pointing instrument with a mean spatial resolution of ~1.5 km and a vertical range gate spacing of 500 m, although instrument oversampling enables 240-m data bins in the *CloudSat* data products. The following products (release R04) are utilized: the 2B geometric profile (2B-GEOPROF), 2B cloud water content–radar only (2B-CWC-RO), 2C precipitation column (2C-PRECIP-COLUMN), and the European Centre for Medium-Range Weather Forecasts auxiliary dataset (ECMWF-AUX). Section 3 describes how these products are used in this study.

The AMSR-E is a passive radiometer on the *Aqua* satellite operating at six dual-polarized frequencies ranging from 6.9 to 89.0 GHz (Kawanishi et al. 2003). The AMSR-E conically scans at a 55° earth incidence angle with a mean spatial resolution of ~5 km for the 89-GHz channel. The version 2-V08 AMSR-E L2A global swath spatially resampled brightness temperatures (Ashcroft and Wentz 2006) and version 2-V06 level-2B global ocean swath (Wentz and Meissner 2004) products were used in this study.

The MHS instrument flies on numerous European Organization for the Exploitation of Meteorological Satellites (EUMETSAT) and National Oceanographic and Atmospheric Administration (NOAA) polar-orbiting platforms and possesses five high-frequency microwave channels between 89.0 and 190.3 GHz. The MHS scans in a cross-track fashion with a mean spatial resolution of ~17 km at nadir.

Data from the AMSR-E and MHS (*NOAA-18* satellite) were collocated with the *CloudSat* observations for this study. *CloudSat* and *Aqua* are members of the "A-Train" satellite constellation, so collocated AMSR-E/CPR observations are readily available. Far fewer collocated MHS/*CloudSat* data points exist, however, since the *NOAA-18* satellite does not fly in a coordinated orbit with *CloudSat*. A combined dataset based on 31 *CloudSat* overpasses between July 2006 and January 2007 was utilized in this study and is described in detail by Chen et al. (2008). The distance between the instrument footprint centers for the vast majority of the observations in the collocated dataset does not exceed 5 km, with most matches on the order of a few kilometers. Even though MHS is a cross-track scanning instrument, the collocated MHS data are all near-nadir observations. The dataset was further quality controlled to include only oceanic observations not affected by sea ice.

3. Methodology

This section describes a combined active/passive modeling system that converts CPR reflectivity factor (hereafter used interchangeably with "reflectivity") observations to simulated multifrequency passive microwave brightness temperatures (T_B).

A few preprocessing steps are first performed to the CPR data. The W-band radar signal can be significantly attenuated due to the combined effects of liquid and melting precipitation, cloud liquid water, large columnar water vapor amounts, and excessive ice water content (IWC). The columnar two-way attenuation for all of these atmospheric constituents is calculated by integrating the layer extinction coefficient downward from the highest *CloudSat* data bin to near-surface levels to create an attenuated-corrected reflectivity profile (see further details later in the section regarding how layer extinction properties are obtained). Attenuation corrections at lower altitudes are generally small for snowfall cases or for typical profiles of ice content associated with midlatitude stratiform precipitation (~1–2 dB) but can be higher for moderate rainfall with elevated freezing levels. The CPR data can also be affected by surface returns in the lowest data bins. Since this study is limited to over ocean observations with a fairly stable clutter pattern, CPR data bins as low as ~500 m AGL are used. Such data bins can be utilized with a clutter reduction algorithm applied to data bins 2–5 in the version 011 2B-GEOPROF product (Tanelli et al. 2008). The CPR reflectivities are also linearly extrapolated to the surface to provide a complete vertical reflectivity profile.

After these preprocessing steps, layer single-scattering properties are calculated. Since a main goal of this study is to investigate simulated T_B uncertainties due to different ice habit models, calculating the scattering characteristics of frozen particles is arguably the most important link in the combined active/passive modeling chain. Above the EMCWF-indicated freezing level, frozen hydrometeor profiles are generated directly from the CPR reflectivity fields via equivalent reflectivity (Z_e) to ice water content conversions. Note the term "ice water content" here refers to the total mass of frozen hydrometeors per unit volume and may be more appropriately labeled "snow water content" in the context of this study.

A priori Z_e–IWC relationships are derived using modeled 94-GHz backscatter properties from the ice particle habits summarized in Table 1, combined with the Field et al. (2005, hereafter F05) ice particle size distribution (PSD) parameterization. The F05 PSD parameterization is derived from airborne measurements of midlatitude frozen PSDs and realistically characterizes the narrow particle concentration peak often observed at smaller particle sizes (e.g., see Figs. 11 and 12 from F05). It also accounts for the inherent temperature dependency of observed in-cloud PSDs. The F05 PSD

TABLE 1. Ice particle model habits and abbreviations from the DDA results of Hong (2007), Kim et al. (2007), and Liu (2008). SS06 frequency-dependent soft spheres and three commonly used variable-density fluffy spheres for snow (FS), graupel (FG), and hail (FH) are also indicated. The coefficient a and exponent b for the respective ice habit m–D relationships [Eq. (2)] are also shown (SI units assumed).

Database	Habit	Abbreviation	a	b
Hong (2007)	Hexagonal column	HC1	0.03	2.00
Hong (2007)	Hollow hex column	HC2	0.02	2.00
Hong (2007)	Hexagonal plate	HP	0.75	2.47
Hong (2007)	6-bullet rosette	HR6	0.18	2.34
Hong (2007)	Aggregate	HA	65.45	3.00
Hong (2007)	Droxtal	HD	347.31	3.00
Liu (2008)	Long hex column	LC1	37.09	3.00
Liu (2008)	Short hex column	LC2	116.12	3.00
Liu (2008)	Block hex column	LC3	229.66	3.00
Liu (2008)	Thick hexagonal plate	LP1	122.66	3.00
Liu (2008)	Thin hexagonal plate	LP2	32.36	3.00
Liu (2008)	3-bullet rosette	LR3	0.32	2.37
Liu (2008)	4-bullet rosette	LR4	0.06	2.12
Liu (2008)	5-bullet rosette	LR5	0.07	2.12
Liu (2008)	6-bullet rosette	LR6	0.09	2.13
Liu (2008)	Sector snowflake	LSS	0.002	1.58
Liu (2008)	Dendrite snowflake	LDS	0.01	1.90
Kim et al. (2007)	Hexagonal column	KC	14.19	2.88
Kim et al. (2007)	4-bullet rosette	KR4	32.30	2.88
Kim et al. (2007)	6-bullet rosette	KR6	47.45	2.88
SS06	Snow (soft sphere)	SS	3.69	3.00
SS06	Graupel (soft sphere)	SG	19.34	3.00
Snow	Snow (soft sphere)	FS	5.26	3.00
Graupel	Graupel (soft sphere)	FG	84.09	3.00
Hail	Hail (soft sphere)	FH	425.71	3.00

scheme relies on moment conversions to obtain the PSD if any moment of the PSD—in this case, the moment of the PSD defined by the layer IWC—is known. The IWC is defined as

$$\mathrm{IWC} = \int m(D)N(D)\,dD, \tag{1}$$

where $m(D)$ is the mass for a given particle size of maximum dimension D and $N(D)\,dD$ the particle concentration. The m–D relationship for frozen particles is represented by

$$m(D) = aD^b, \tag{2}$$

where a and b are dependent on the ice particle models shown in Table 1. For a given set of input IWC values, the PSD can be derived based on the b moment of the PSD defined by Eqs. (1) and (2) (e.g., Field et al. 2007; Kim et al. 2007; Thompson et al. 2008; Kulie and Bennartz 2009), and Z_e for a given IWC value is calculated by integrating particle backscatter cross sections from the ice models in Table 1 over the derived PSD. The Hong (2007), Kim et al. (2007), and Liu (2008) ice habit models are nonspherical with single-scatter properties (e.g., volume extinction, single-scattering albedo, and asymmetry factor) calculated using the discrete dipole approximation (DDA) (Draine and Flatau 1994) assuming randomly oriented particles, whereas the Surussavadee and Staelin (2006, hereafter SS06) models are spherical with frequency-dependent effective particle densities for snow and graupel. Three other variable-density spherical models shown in Table 1 for snow, graupel, and hail are also included in the database. Such "soft" or "fluffy" spheres have been used extensively for microwave remote sensing applications and are standard ice particle models, for example, embedded within the Joint Center for Satellite Data Assimilation's Community Radiative Transfer Model (Han et al. 2006).

Figure 1 highlights Z_e–IWC relationships for an assumed temperature of −7.5°C. These relationships are temperature dependent and are derived for 11 temperature bins at 5°C intervals between −2.5° and −57.5°C to account for PSD differences modulated by temperature (F05). Figure 2 shows derived PSDs for a representative sample of the ice models from Table 1. Note that an input radar reflectivity factor of 10 $\mathrm{mm}^6\ \mathrm{m}^{-3}$ is assumed in Fig. 2 for illustrative purposes. Since the derived IWC for a given Z_e is different for each ice model, the derived PSD also differs. The PSDs are also strongly modulated by the m–D relationships outlined in Table 1. For instance, some of the ice particles displaying elevated a coefficients and/or b exponents (e.g., some of the columns, plates, and droxtals) produce PSDs that are skewed heavily toward lower particle sizes, whereas other ice models with lower exponent b values nearer 2.0—and thus more representative of observed aggregate particles (e.g., Locatelli and Hobbs 1974; Brown and Francis 1995; Mitchell 1996)—trend toward larger particle sizes for the same input Z_e value. The ramifications of these PSD differences will be discussed in section 6.

CloudSat data products are used to generate profiles of other quantities needed to calculate layer extinction properties for RT simulations. Profiles of temperature, pressure, and water vapor content (WVC) are obtained from the ECMWF-AUX product. Cloud liquid water content (LWC) profiles from the 2B-CWC-RO product (Austin 2007; Chen et al. 2008) are utilized in nonprecipitating regions. The LWC and WVC profiles are scaled by their collocated AMSR-E retrieved columnar liquid water path (LWP) and water vapor path (WVP) values. This scaling is performed to obtain improved emission

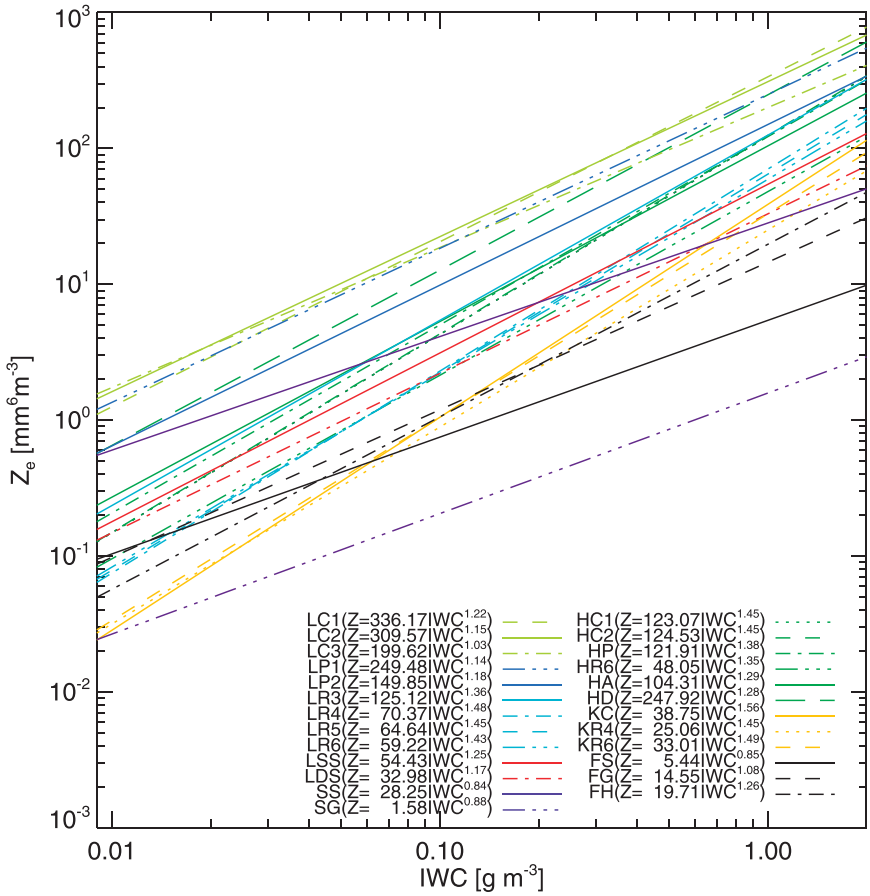

FIG. 1. Derived Z_e–IWC relationships (94 GHz) for 25 ice particle models and the F05 PSD for the −7.5°C temperature bin. Abbreviations for the ice particle models can be found in Table 1.

signature simulations at the scale of the passive microwave observations so the scattering effect of ice particles can be better isolated. In precipitating regions below the freezing level, CPR reflectivity data are converted to rainfall rates (R) using Z_e–R relationships developed for W-band radars (L'Ecuyer and Stephens 2002). AMSR-E LWP retrievals are also used to supplement the *CloudSat* 2B-CWC-RO LWC retrievals since the 2B-CWC-RO LWC retrievals are unusable in precipitating conditions. AMSR-E LWP values are distributed evenly in those data bins containing unphysical (and thus flagged) 2B-CWC-RO LWC solutions to vertically distribute cloud liquid water. Layer gaseous (e.g., water vapor, nitrogen, oxygen) and cloud liquid water absorption are respectively derived using the Rosenkranz (1998) and Liebe et al. (1991) algorithms. Liquid precipitation absorption and scattering properties are generated using standard Mie theory after applying appropriate fall speed assumptions suitable for rain and are averaged over an assumed rain drop size distribution (e.g., Bennartz and Petty 2001). It should be noted that a melting layer model is currently not employed to account for partially melted particles. The implications of this deficiency are discussed later in the manuscript.

Layer extinction properties due to gaseous absorption and cloud liquid water are combined with PSD-averaged hydrometeor extinction properties as input for RT simulations. Ocean surface emissivities are modeled using version 2 of the Fast Emissivity Model (FASTEM-2) (DeBlonde and English 2001), and all RT calculations are performed with the slant-path version of the successive order of interaction (SOI) RT model (Heidinger et al. 2006; O'Dell et al. 2006) for the following frequencies: 6.9, 10.6, 18.7, 23.8, 36.5, 89.0, and 157.0 GHz. This frequency subset is particularly relevant for the upcoming Global Precipitation Measurement (GPM) mission that will operate a microwave imager at similar frequencies, and current observations from AMSR-E and MHS are available for these frequencies. All SOI simulations are performed using eight streams. The expected SOI T_B error at higher frequencies under highly scattering conditions should not exceed ~0.1 K using

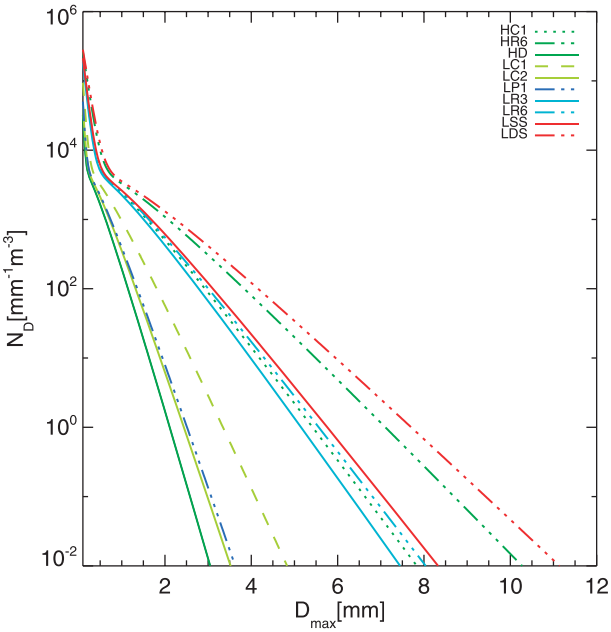

FIG. 2. PSDs derived for the ice particle models indicated in the legend using the F05 parameterization. An input radar reflectivity factor of 10 mm^6 m^{-3} is assumed.

eight streams (Heidinger et al. 2006). Two sets of simulations for each profile are performed using an assumed 55.1° (AMSR-E) and 0° (MHS) zenith angle. Modeled results are convolved to the approximate passive microwave footprints along the *CloudSat* path for comparison purposes as a first-order correction for footprint mismatches between the higher resolution *CloudSat* data and the lower footprint resolution of the various passive microwave sensors. This convolution procedure is most appropriately suited for larger-scale precipitating systems, and the results presented in this study concentrate on such frontal precipitation events.

4. Case study results

a. Overview

A synoptic precipitation event is presented to highlight the active/passive modeling system and offer an assessment of the ice particle models. This oceanic case study was observed between Australia and Antarctica near 0400 UTC 9 August 2006 (*CloudSat* orbit 01497). Figure 3a depicts extensive clouds and precipitation associated with a large frontal system. Cloud-top heights are between 8 and 10 km; maximum CPR reflectivities are between 10 and 15 dBZ_e in the cold sector and 15–20 dBZ_e in the warmer, raining locations. An interesting feature of this particular *CloudSat* overpass is the transition from frozen to liquid precipitation coinciding with a freezing level increase from 0 to 2 km near 57.5°S latitude. Obvious brightband features accompany this transition and confirm the existence of liquid hydrometeors below 2 km AGL. [The term "brightband" is used throughout this paper to denote the increased reflectivity associated with the melting level. Note, however, that the physical mechanism responsible for increased reflectivity signatures accompanying the melting level at 94 GHz differs from the well-documented peak reflectivity associated with melting particles at lower frequencies (e.g., Sassen et al. 2007).] With the exception of some liquid clouds near 60°S, retrieved LWP values are very low in the snowfall regions (Fig. 3f). LWP increases north of the transition zone, with numerous LWP maxima exceeding 0.2 kg m^{-2} coinciding with near-surface reflectivity maxima.

Figures 3b through 3e show AMSR-E observations for the vertically polarized (V) 36- and 89-GHz channels, as well as MHS observations at 89 and 157 GHz. These observations indicate warmer T_Bs at all frequencies coincident with liquid clouds and precipitation and lower T_B values between ~59° and 57°S in snowing regions due to reduced LWP and enhanced scattering from frozen hydrometeors.

b. Validity of ice particle models

Simulation results using the ice habits from Table 1 are also overlaid in Fig. 3 revealing the T_B sensitivity to ice particle properties. The most obvious feature in the simulation results is the large deviation from observations associated with certain ice models. For instance, the Hong (2007) and Liu (2008) (hereafter referred to as the "DDA" ensemble containing 17 ice models) 36V simulation results realistically follow the AMSR-E observations (Fig. 3b). Since the 36V channel is most sensitive to LWP emission and not as susceptible to scattering as higher-frequency channels, sensitivity to the various ice particle models is not expected. However, all spherical and some nonspherical models deviate from the observations in the snowfall regions when the columnar ice water path (IWP) reaches a critical level. Similarly, the emission signals revert to T_B depressions in high-LWP regions (Fig. 3f) for these same ice models. This trend is magnified at higher frequencies (Figs. 3c–e) with large simulated T_B depressions in precipitating regions. Conversely, the simulated T_Bs from the Hong (2007) and Liu (2008) models produce physically realistic results for all frequencies. Similar discrepancies between the ice models are pervasive throughout the entire dataset for precipitation events. Note that the nonweighted DDA ensemble average T_Bs for each frequency is indicated by a solid gray line in Figs. 3b–e. The ±1 standard deviation

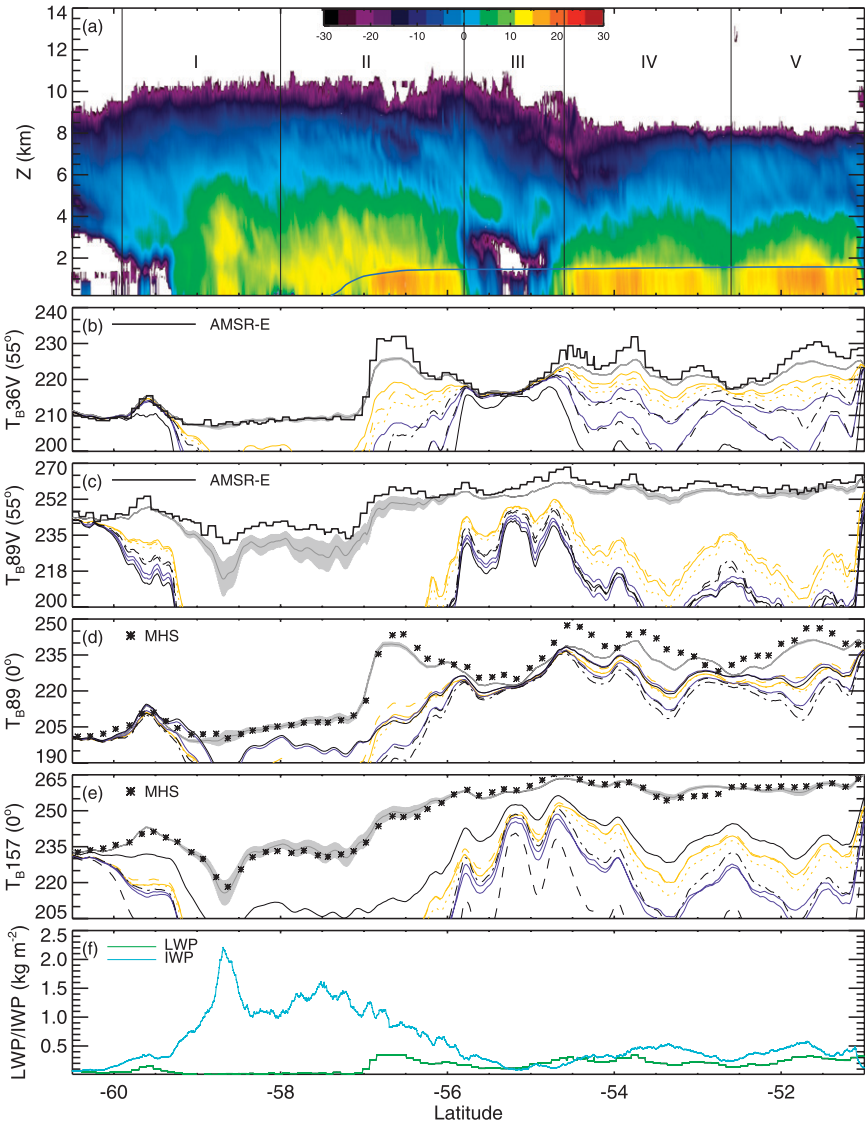

FIG. 3. (a) Attenuation-corrected CPR reflectivity and freezing level (blue line) from *CloudSat* orbit 01497. (b)–(e) Brightness temperature (K) for the following instruments and channels (black lines/asterisks): (b) AMSR-E 36V and (c) 89V GHz; (d) MHS 89 and (e) 157 GHz. (f) AMSR-E derived LWP (green) and IWP (blue) derived from the DDA ensemble results. Simulated T_Bs for the DDA ensemble and 1-σ uncertainties (light gray shading), as well as spherical and Kim et al. (2007) models (using the same color scheme as in Fig. 1) are also included in (b)–(e). Also, (a) shows five separate zones that are used for calculating the individual ice habit biases in Fig. 8.

(1σ) of the DDA ensemble simulated T_B is also highlighted by the gray shading.

The cause of the simulated T_B discrepancies is due primarily to the following two effects related to differences in the scattering properties of the ice models: 1) Z_e–IWC relationships and 2) extinction properties. The first link in the modeling system uses backscatter properties for each ice model to convert CPR reflectivities to IWC using Z_e–IWC relationships. Figure 4 compares the derived IWP from two "fluffy" spherical models (FS and FG, Table 1)—as well as the KR6 habit and DDA ensemble average—for the precipitation event shown in Fig. 3. The IWP derived from the low-density snow model (FS) consistently exceeds the DDA-derived IWP by about two orders of magnitude due to the Z_e–IWC relationships shown in Fig. 1. For a given CPR reflectivity, the FS-derived IWC is much larger than the DDA-derived IWC owing to comparatively smaller backscatter

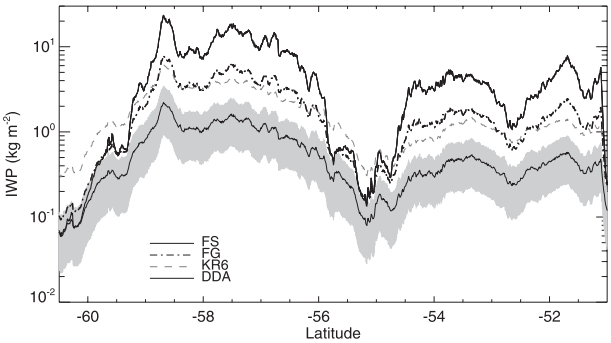

FIG. 4. Derived ice water path (kg m^{-2}) for fluffy spheres (FS), graupel (FG), and the Kim et al. (2007) six-arm rosette (KR6). The DDA ensemble average (solid gray line) and 1-σ uncertainty results (light gray shading) are also shown.

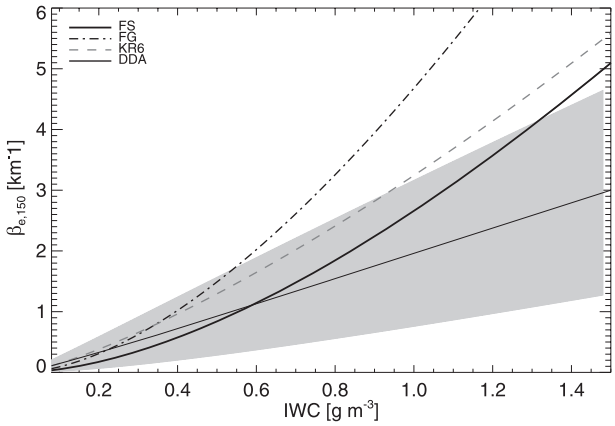

FIG. 5. Simulated volume extinction coefficient (km^{-1}) as a function of IWC (g m^{-3}) for the same ice habits indicated in Fig. 4. The DDA ensemble average (solid gray line) and 1-σ uncertainty results (light gray shading) are also shown.

cross sections of the low-density spherical model at all particle sizes (not shown) that strongly affect the Z_e–IWC relationships. The inflated layer IWC retrievals cumulatively produce excessive column-integrated IWP and are the primary reason for the large simulated T_B depressions due to intensive scattering.

The higher-density graupel spherical model (FG) and the KR6 habit also exceed the DDA ensemble average IWP—and the upper IWP limit defined by the DDA ensemble uncertainty—by a smaller, yet still significant, margin compared to the FS habit (the large derived IWP uncertainty exceeding that of the DDA ensemble by ~60% will be highlighted in section 6). However, these particles also exhibit larger PSD-averaged extinction properties for a given IWC compared to the DDA ensemble average (Fig. 5). The combination of elevated retrieved IWP and increased extinction are therefore both significant factors contributing to reduced simulated T_Bs for the FG and KR6 models. The volume extinction coefficients for these ice models reside within the uncertainty range of the DDA ensemble at lower IWC amounts and only exceed the DDA ensemble envelope at larger IWCs, so the PSD-averaged extinction properties do not differ as dramatically from the DDA ensemble compared to the FS backscatter properties. Note also the reduced extinction properties of the FS model in Fig. 5 compared to the DDA ensemble average, thus confirming the dominant role of the Z_e–IWC relationships—not extinction properties—in producing excessive scattering for this ice model.

c. Simulation uncertainties and errors

Since the relative validity of the DDA ensemble has been established, only DDA results are shown in Fig. 6 to highlight the 1-σ simulation uncertainties at each frequency. Simulated T_B36V uncertainties are low (<0.75 K) for this emission-sensitive channel, with excellent comparisons to ASMR-E T_B36V observations in the snowfall sector due to low LWP values in this region (Fig. 3b). Note, however, the excellent agreement between simulation results and observations near the LWP maximum located at ~59.7°S associated with a shallow liquid cloud feature—an expected result since the model LWP is directly scaled to AMSR-E-derived LWP. In the raining regions, however, there are several areas of negative T_B36V bias where the model underestimates emission.

Larger simulated T_B89V uncertainties display a functional relationship with IWP and range from 4 to 9 K in the snowing regions (Fig. 6), indicating stronger sensitivity of this channel to the scattering properties of the different ice models in higher-IWP regions. Simulated T_B89V uncertainties in the warm sector of the synoptic weather system are generally around 2–3 K. The simulated T_B89V results are consistently biased low (up to ~14 K, but with large uncertainties) when compared to AMSR-E observations—but are not egregiously low

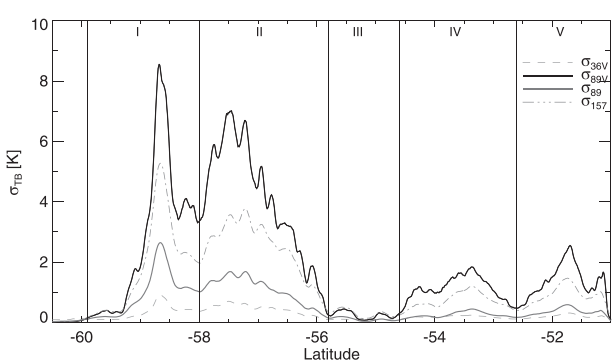

FIG. 6. Simulated T_B uncertainties for 36V (light dashed), 89V (dark solid), 89 GHz (light solid), and 157 GHz (light dashed–dotted). The five separate zones from Fig. 3a are also indicated.

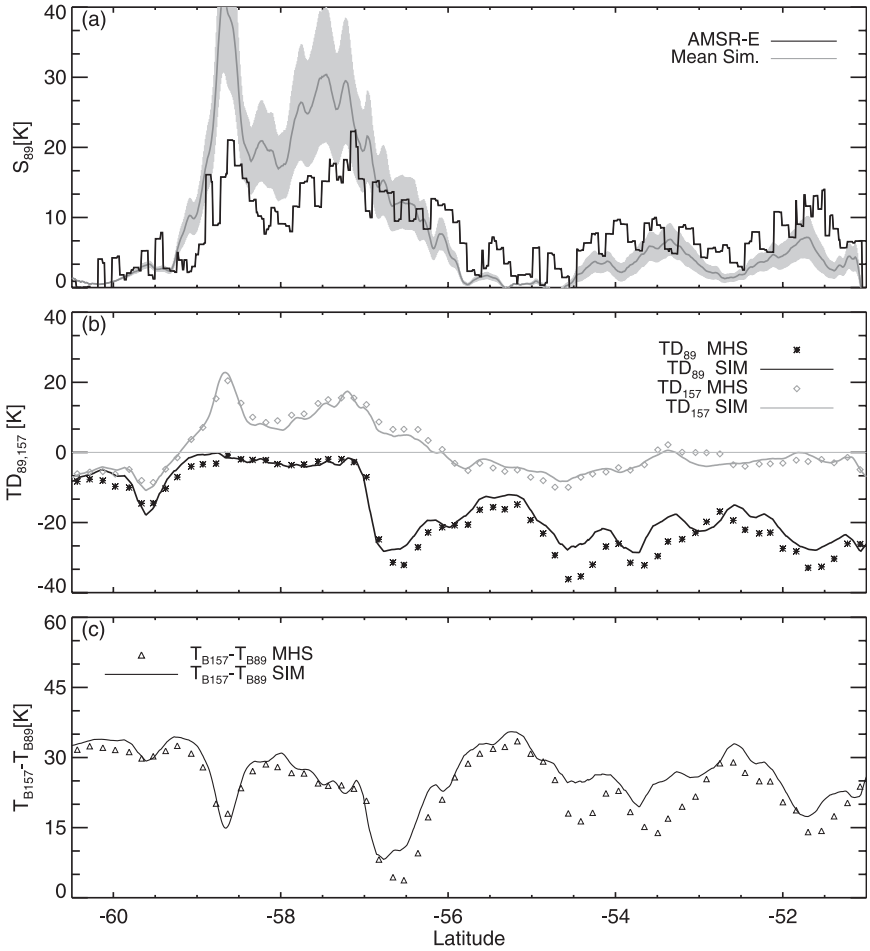

FIG. 7. (a) AMSR-E (dark) and simulated (light) scattering index for 89 GHz (K), (b) MHS 89 (dark asterisk)–157-GHz (light diamond) and simulated 89 (dark solid line)–157-GHz (light solid line) brightness temperature depression (K) compared to water vapor-only results, and (c) MHS (triangles) and simulated (solid line) 157–89-GHz brightness temperature difference (K). The latitude domain corresponds to Fig. 3.

like the spherical model results (Fig. 3). As shown in Fig. 7a, the simulated 89-GHz scattering index (S_{89}) (Petty 1994) indicates excessive scattering in the snowfall region. Vertical (V) and horizontal (H) polarization information from the 89-GHz channels—combined with estimates of T_B89V/H in nearby cloud-free regions—are used to calculate S_{89} to estimate the T_B depression due to scattering by frozen particles. Simulated S_{89} values exceed those derived by AMSR-E observations by a factor of 2 over much of the snowfall region. The simulated S_{89} values are not inflated in the liquid precipitation regions (Fig. 7a), while simulated T_B89V values in these same regions are consistently lower than observed values (Fig. 3c), thus hinting at emission underestimation similar to the 36V results.

The satellite zenith angle also needs to be considered when characterizing simulated T_B uncertainties. In contrast to 89V results with an oblique satellite viewing angle, the MHS 89-GHz near-nadir observations and simulated results display a much lower sensitivity to frozen hydrometeors and only respond to emission from LWP (Fig. 3d). Simulated T_B89 uncertainties are generally around 1–2 K in the snowfall region and are negligible elsewhere (Fig. 6). This lack of sensitivity to IWP is also emphasized by no discernible T_B89 depression when compared to cloud-free RT simulations (Fig. 7b).

The 157-GHz MHS observations and simulated T_Bs display obvious sensitivity to IWP at near-nadir viewing angles. There are noticeable T_B157 minima coinciding with high IWP values (Fig. 3e), simulated T_B157 uncertainties are between 2 and 5 K in these same regions (Fig. 6), and T_B157 depressions compared to cloud-free simulations are readily apparent (Fig. 7b). Additionally, differences in T_B157 and T_B89 emphasize the enhanced

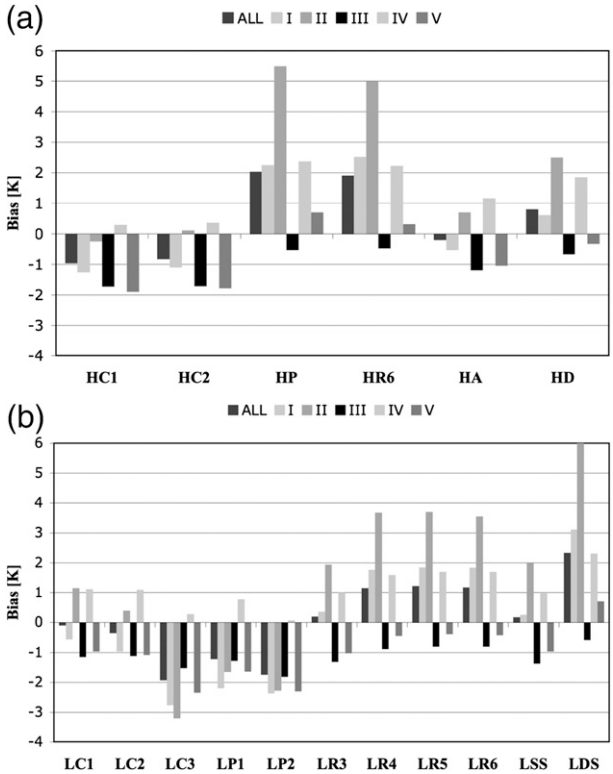

FIG. 8. Simulated vs observed 157-GHz brightness temperature bias (K) corresponding to the case study illustrated in Fig. 3a. The "All" column refers to the entire latitudinal domain shown in Fig. 3; the other columns (I, II, II, IV, V) refer to the regional subsets indicated in Fig. 3a. The ice habit labels follow the same nomenclature as Table 1.

sensitivity of the 157-GHz channel to the IWP (Fig. 7c). Unlike the 89V results, comparisons between MHS and simulated T_B157 are excellent and exhibit relatively low bias in the highest scattering regions (Fig. 3e). Also note the higher simulated 89V versus 157-GHz uncertainties due to viewing angle effects (Fig. 6).

d. Individual ice particle model comparisons

Some of the Hong (2007) and Liu (2008) ice habits (e.g., columns, plates, droxtals, simple rosettes, etc.) are probably not intended as realistic proxies for precipitation-sized ice particles, but rather for smaller ice habits commonly observed in higher-level ice clouds. To justify using an ensemble containing all of these habits to calculate model uncertainties in precipitating regions, Fig. 8 shows simulated versus observed T_B157 biases for the case study. A few ice habits demonstrate very low biases (<0.3 K) across the entire precipitating system between ~60° and 51°S (i.e., the "All" column in Fig. 8), specifically the LC1, LSS, LR3, LC2, and HA models. Note, however, the extreme variability in simulated biases when regional subsets (labeled I–V in Fig. 3a) are considered. These may indicate fundamental changes in scattering properties of the frozen particles in different sections of the synoptic weather system. For instance, the HR6 model has one of the higher bias values (~1.9 K) over the entire domain, but displays the lowest biases in region III and V. The LP2 shape exhibits typical biases near 2 K in all other areas except region IV, where its bias is very low. The variability of these results seems to justify using an ensemble populated by the entire Hong (2007) and Liu (2008) dataset since the combined active/passive properties of even the pristine crystal habits compare well in the precipitating regions. However, other error sources not related to the scattering properties of the ice models could also affect the results in Fig. 8. The 157-GHz channel, however, should be substantially less sensitive to error sources from lower atmospheric levels in the presence of adequate IWP (e.g., Bennartz and Bauer 2003). This trait is highlighted in Fig. 7b, which shows the enhanced sensitivity of the nadir 89-GHz channel to emission in the high-LWP regions. Conversely, the 157-GHz results do not display large peaks in the same regions because of enhanced scattering by ice particles aloft, and the biases reflected in Fig. 8 are presumably more immune from error sources other than the ice particle model.

e. Summary of case study results

In summary, the case study highlights the following issues:

- Spherical models produce unrealistic simulated T_B results, while certain nonspherical (DDA) models are physically consistent
- IWP retrieval uncertainty exceeds 60% for the DDA ensemble
- High (low) sensitivity of the 89V–157 nadir (36V–89 nadir) channels to IWP
- Large simulated T_B89V (up to 9 K) and T_B157 (up to 5 K) uncertainties
- Excellent agreement between simulations and observations for 36V, 89, and 157 GHz in the snowfall region, but excessive simulated T_B89V depressions
- Negative simulated T_B biases at all frequencies in the rainfall region
- Highly variable simulation-MHS T_B157 comparisons for the different ice particle models in subregions of the synoptic weather system

5. Global results

a. Statistical comparison by precipitation type

In this section, results from the entire collocated *CloudSat*/AMSR-E/MHS dataset are tabulated by

TABLE 2. Description of the different cloud and precipitation categories used for simulation vs observation comparisons. Abbreviations used to denote the categories in various figures and tables are also indicated. The number of *CloudSat*/AMSR-E/MHS coincident observations for each category (N_{obs}) used to generate the statistics in Fig. 9 is also shown.

Cloud/precip category	Label	N_{obs}	Description
All clouds	AC	9043	All clouds, no precipitation.
Cold clouds	CC	2494	Cold clouds only (<0°C), no precipitation.
Warm clouds	WC	2894	Warm clouds only (>0°C), no precipitation.
All precipitation	AP	5153	All precipitation occurrences.
Stratiform (midlat)	SML	1911	Mid-latitude (lat > |30°|) stratiform precipitation.
Stratiform (low FL)	SLFL	916	Mid-latitude stratiform, freezing level (FL) < 1 km.
Stratiform (high FL)	SHFL	583	Mid-latitude stratiform, FL > 1 km.
Stratiform (brightband)	SBB	412	Mid-latitude stratiform with obvious brightband.
Low-topped convection	LTC	1148	Shallow, higher latitude (lat > |45°|) convection.

different criteria to demonstrate variability to cloud or precipitation type. Table 2 shows the cloud and precipitation categories, as well as the number of collocated *CloudSat*/AMSR-E/MHS observations associated with each category used to calculate the statistics displayed in Fig. 9. Precipitation classification was performed manually/visually based on the *CloudSat* swaths and auxiliary temperature information. Since this study focuses on precipitation and since Chen et al. (2008) provides a detailed examination of RT validation based on many additional cloud categories from the *CloudSat* products, only three basic nonprecipitating cloud categories are indicated in Table 2. Note that the "cold" cloud category is defined very broadly and, in addition to ice clouds, this category may also include clouds comprised of supercooled water.

Statistics for the various cloud and precipitation types are shown in Fig. 9. These statistical measures [bias, bias-corrected rms error (RMSE), and average T_B uncertainty] are defined with respect to simulations versus observations. Linear correlation coefficients were also calculated and almost universally exceeded 0.90–0.95 without marked variability (not shown). The average T_B uncertainty ($\overline{\sigma}$) is the standard deviation between the T_B results for the different ice models and is thus a measure of the spread between the different simulations. As illustrated in the case study, there are notable differences between the spherical and DDA ensembles. The spheres consistently produce large biases and RMS errors, low correlations, and very large $\overline{\sigma}$ values for the entire collocated dataset (not shown). The remaining analysis and discussion will therefore focus exclusively on the DDA ensemble results shown in Fig. 9.

For clear-sky cases all frequencies exhibit low biases, correlations exceeding 0.95, and low RMSE values, indicating that clear-sky atmospheric and ocean surface properties are well modeled. The cloud categories contain relatively small negative biases and similar statistical results. The global DDA results, however, display trends dependent on frequency and precipitation type. Highlights of the global DDA ensemble results from Fig. 9 include

- distinct statistical differences between precipitation categories, especially the simulated T_B uncertainties
- stratiform brightband events display the largest negative biases, while negative biases of 3–4 K exist for many precipitation categories
- distinct viewing angle differences between 89V and 89 nadir results
- lower 157-GHz biases (−1 to −1.5 K) compared to other frequencies for most precipitation categories, most likely due to scattering effects that modulate emission from below the freezing level

The average simulated T_B uncertainties ($\overline{\sigma}$) shown in Fig. 9c mimic the test case results with their dependence on frequency and also highlight differences between precipitation categories. Simulated σ_{36V} are very low due to decreased sensitivity of this channel to scattering effects, whereas σ_{89V} has higher values exceeding 1 K for most categories and 2.5 K for the brightband cases. The σ_{89} nadir values are consistently below ~0.6 K except for the brightband category (~0.9 K). The σ_{157} nadir values display substantial variability between the precipitation categories with the brightband events possessing the highest average simulated T_B uncertainty (1.8 K). Also note that simulated T_B uncertainties are generally much lower than rms errors, indicating that the models display increased similarity to each other compared to the observations.

b. Dependence on ice content

The average T_B uncertainties presented in Fig. 9 are useful to illustrate the sensitivity of simulated results to the ice particle model, but they should be analyzed with caution since these uncertainties exhibit a functional dependence on IWP (Fig. 6). Since IWP retrievals are dependent on the ice model, an integrated reflectivity

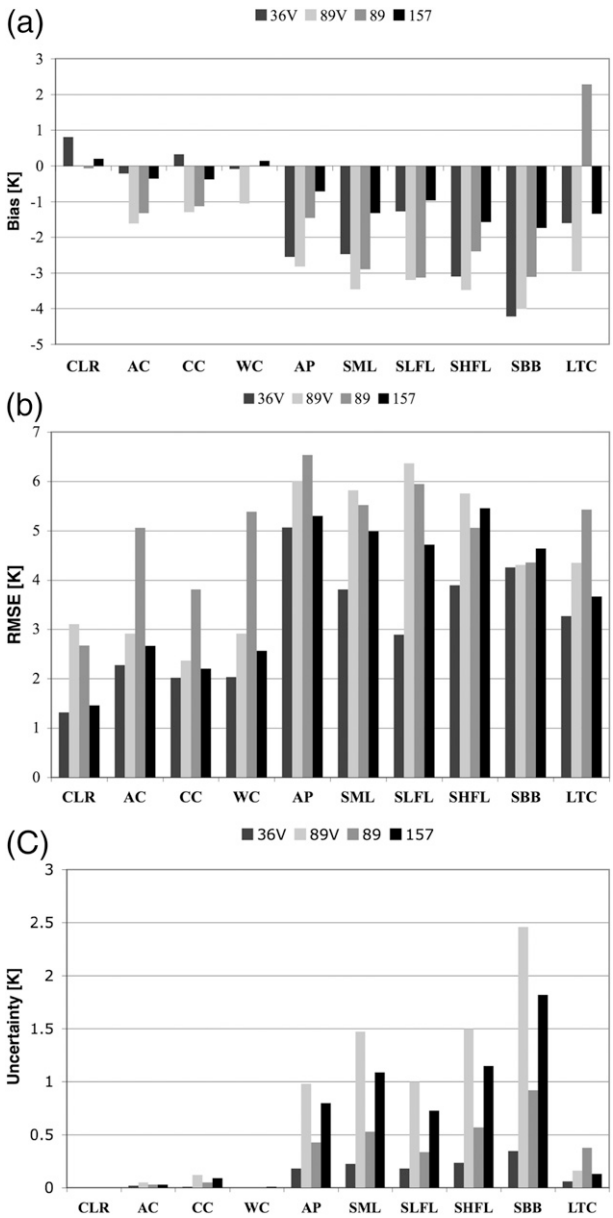

FIG. 9. Simulated DDA ensemble brightness temperature vs AMSR-E/MHS (a) bias, (b) bias-corrected RMSE, and (c) average simulated T_B uncertainty ($\overline{\sigma}$) for different cloud and precipitation categories. Abbreviations for the cloud and precipitation categories can be found in Table 2.

quantity (Z_{int}, mm^6 m^{-2}) is introduced as a proxy for IWP:

$$Z_{\mathrm{int}} = \int_{H_{\mathrm{FL}}}^{H_{\mathrm{CT}}} Z_{\mathrm{CPR}}(z)\, dz, \tag{3}$$

where Z_{CPR} is the attenuation-corrected CPR reflectivity at a given height z and H_{FL} and H_{CT} are the respective freezing level and cloud-top height: Z_{int} is a useful metric since it conveys a vertically integrated

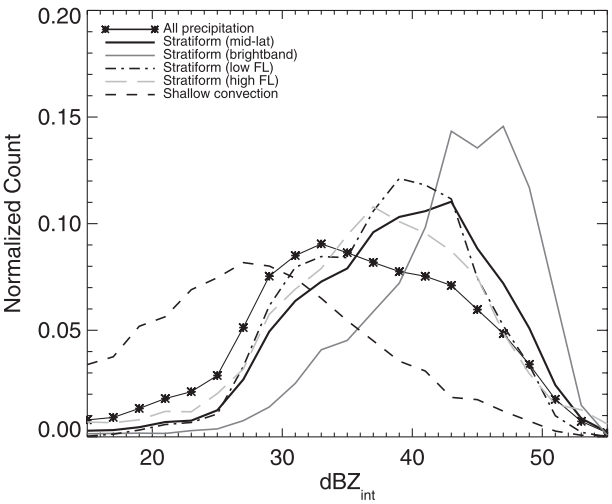

FIG. 10. Histograms of column-integrated reflectivity above the freezing level (dBZ) for different precipitation categories in 2-dB bins.

property above the freezing level, yet is independent of the ice habit model. Histograms of Z_{int} are shown in Fig. 10 and indicate disparities between precipitation categories. For instance, ''all precipitation'' peaks near 30 dBZ_{int}, while the various stratiform subcategories display higher, but variable, peaks in their Z_{int} distributions. Most notably, the ''stratiform brightband'' category possesses the highest Z_{int} maxima compared to all other midlatitude stratiform categories.

Figure 11 illustrates 157-GHz simulation biases for the individual habits in the DDA ensemble as a function of Z_{int} for all midlatitude stratiform observations. The bias magnitudes are consistently low ($\lesssim$1 K) below the 35-dBZ_{int} data bin. There is also minimal spread in the bias results among the various ice particle models below this threshold, so the ice particle model employed is not particularly crucial until a critical Z_{int} level is reached. There is considerable divergence in the results above the 35-dBZ_{int} threshold, and numerous ice particle models exhibit large negative biases owing to excessive scattering when dBZ_{int} exceeds about 45. In contrast to the case study results, a few ice models produce more consistent results across the entire Z_{int} spectrum (e.g., HP, HR6, and LDS), while others become outliers at the highest Z_{int} levels (e.g., HC1, HC2, HA, LC2, LC3, LP1, and LP2). The number of midlatitude stratiform observations is reduced above ~45 dBZ_{int}, so the statistics above this threshold are not as robust. Nonetheless, these results indicate potential systematic errors in the scattering properties for many of the DDA ensemble members at high Z_{int} levels, so the veracity of some ice models for microwave remote sensing of high-IWP precipitation events remains questionable.

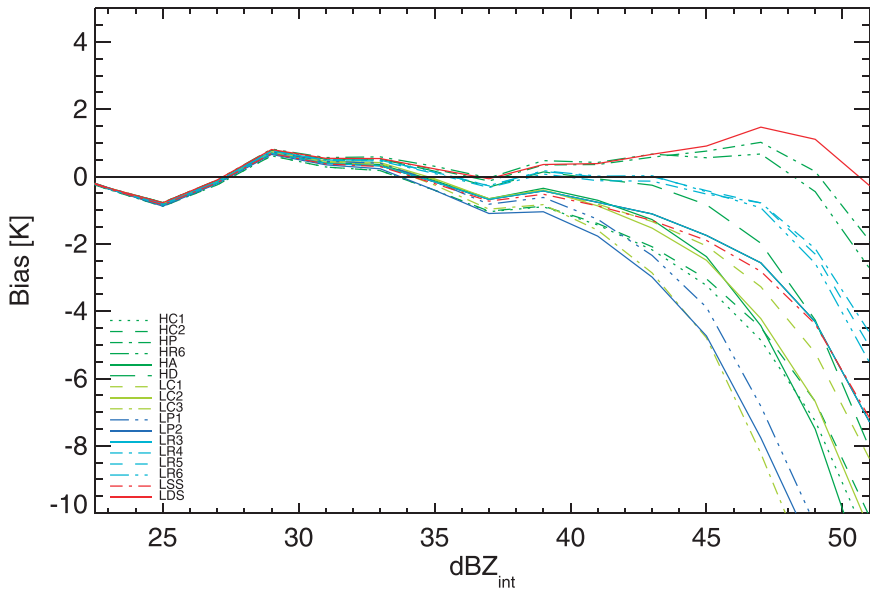

FIG. 11. Simulated vs observed 157-GHz brightness temperature bias (K) using the DDA ensemble of ice particle models for the midlatitude stratiform precipitation category.

To investigate simulated T_B uncertainty differences among the precipitation categories due to average columnar ice properties, Fig. 12 shows σ_{157} for different selected values of Z_{int} based on best-fit lines between these two quantities (not shown). As Fig. 12a indicates, the differences in σ_{157} are not wide among the stratiform categories at lower Z_{int} levels, but larger variations occur at higher Z_{int} data bins. The bias-corrected RMSE values for 157 GHz are also shown in Fig. 12b. When used in combination with the results from Fig. 12a, the T_B uncertainties due to scattering characteristics of the ice models contribute significantly to the overall model error variability at the highest Z_{int} values, while other model error sources appear to dominate the error variability at lower Z_{int} levels—especially for the "all precipitation" category.

c. *Error correlations/covariances*

To illustrate the utility of the combined active/passive modeling results to data assimilation applications, error correlations and covariances for the lower and higher freezing level midlatitude stratiform precipitation categories are shown in Tables 3 and 4. Model errors are defined as the average simulated ensemble T_B subtracted from the observed T_B for each frequency. Since the dependence of simulated T_B uncertainties on Z_{int} has already been demonstrated, these tables only consider results from the 40-dBZ_{int} data bin. The off-diagonal elements of such error covariance matrices influence how the observations are utilized in data assimilation schemes, yet are difficult to characterize under precipitating conditions. Tables 3 and 4 combine the error correlations (upper right half of the matrix) and covariances (lower left half of the matrix, including the diagonal elements). The complete observational error matrix would contain all

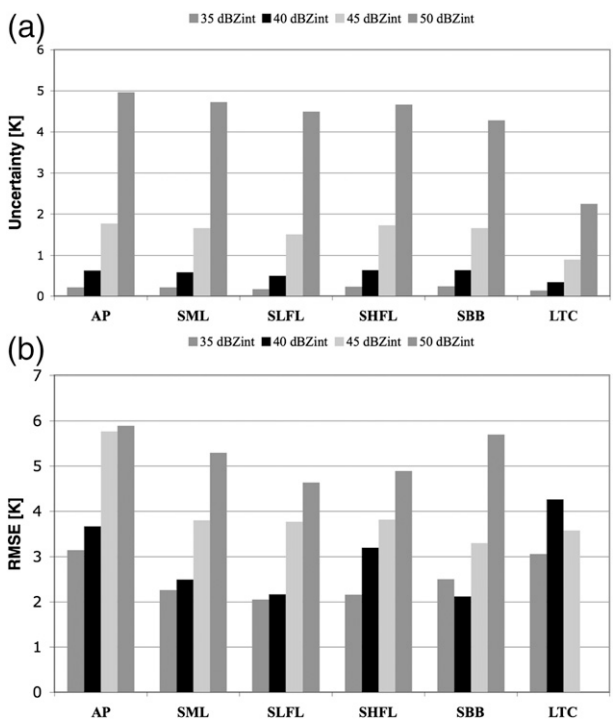

FIG. 12. (top) Simulated T_B157 uncertainty (K) and (bottom) bias-corrected RMSE (K) as a function of Z_{int} for the different precipitation categories listed in Table 2.

TABLE 3. Lower freezing level midlatitude stratiform precipitation model error covariances (K^2) (boldface, lower left half) and correlations (upper right half) from the 40-dBZ_{int} data bin for the following frequencies: 18V, 23V, 36V, 89V, and 157 GHz.

	18V	23V	36V	89V	157
18V	**1.99**	0.85	0.74	0.06	0.25
23V	**1.70**	**1.99**	0.75	0.13	0.24
36V	**1.42**	**1.44**	**1.84**	0.13	0.11
89V	**0.18**	**0.43**	**0.40**	**5.21**	0.41
157	**0.80**	**0.75**	**0.33**	**2.13**	**5.13**

TABLE 4. As in Table 3 but for higher freezing level midlatitude stratiform precipitation.

	18V	23V	36V	89V	157
18V	**4.51**	0.93	0.82	0.07	0.13
23V	**3.52**	**3.17**	0.81	0.05	0.09
36V	**5.86**	**4.87**	**11.39**	0.31	0.13
89V	**0.57**	**0.35**	**4.17**	**15.79**	0.55
157	**0.60**	**0.35**	**1.00**	**4.99**	**5.15**

microwave channels, but only the vertically polarized channels are indicated in Tables 3 and 4 for brevity. Lower-frequency channels are also not illustrated owing to their low sensitivity to ice particle model. Since 157-GHz observations containing polarization diversity at an AMSR-E-like viewing angle are not available, the nadir results are assumed to realistically represent the error correlations/covariances.

The error correlations and covariances shown in Tables 3 and 4 again highlight the importance of partitioning the results between different precipitation types. Error correlations exceed 0.75 between all of the lowest three channels (18, 23, and 36 GHz) in both precipitation categories, with the higher freezing level category displaying slightly increased correlations at these frequencies. Note, however, that the covariances for these same channels display marked differences between the two precipitation categories. For instance, the 36V variance increases from 1.84 (low freezing level) to over 11 K^2 (higher freezing level). Error correlations between the 89/157-GHz channels and the lower three frequencies are consistently lower, although the 36V–89V error correlation increases from 0.13 (low freezing level) to 0.31 (high freezing level). The error correlations between 89V and 157 are much higher than the 89V–157 error correlations with lower frequencies. The higher freezing level category also has a noticeably higher 89V–157 error correlation than lower freezing level events, while a large 89V covariance disparity exists between the two precipitation categories. Figure 13 also highlights 89V–157 and 89V–36V error correlation differences—and 157-GHz variance calculations—as a function of Z_{int} for three different precipitation categories. The midlatitude stratiform categories display mostly similar 157–89V error correlation trends and magnitudes, but there are larger discrepancies evident at certain Z_{int} data bins. The shallow convective precipitation 157–89V error correlations, however, diverge strongly from the stratiform categories below the 40-dBZ_{int} data bin. Considerable variability also exists between the three precipitation types in the 89V–36V error correlations. Similar to Fig. 12, the 157-GHz variances exhibit a Z_{int} dependency and are dictated by enhanced scattering effects at the highest Z_{int} levels (Fig. 13c). Note that the variances in Fig. 13 link the error correlations with covariances shown in Tables 3 and 4.

6. Summary and conclusions

This study describes a combined active/passive microwave modeling system that converts *CloudSat* CPR reflectivity fields to multifrequency passive microwave brightness temperatures (T_B). The hydrometeor profiles provided by the CPR are particularly beneficial, and

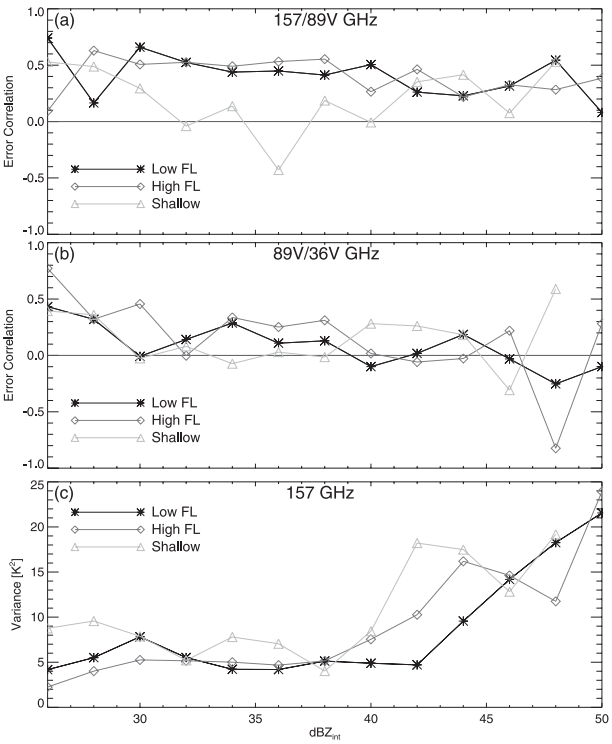

FIG. 13. (a) 157–89V and (b) 89V–36V show error correlations for three different precipitation categories as a function of integrated reflectivity above the freezing level (Z_{int}). (c) Error 157-GHz error variances for the same precipitation categories. The low freezing level midlatitude stratiform (Low FL), higher freezing level midlatitude stratiform (High FL), and higher latitude, shallow convective precipitation categories are shown (see Table 2).

CPR observations also allow the variability of the results to be studied by precipitation classification. This modeling system also constrains the physical properties of frozen hydrometeor models, requiring both backscattering (converting Z_e to IWC to derive the PSD) and extinction (calculating PSD-averaged properties for passive microwave RT simulations) properties to be self-consistent for realistic results to be obtained from both an active and passive perspective.

Since scattering by frozen hydrometeors produces the primary higher-frequency passive microwave precipitation signature and is a large source of uncertainty in forward models, this study illustrates the sensitivity of simulated results to the choice of ice particle model. Synoptic precipitation case study results, as well as globally averaged results, indicate that certain ice particle models (e.g., low-density spheres) produce consistently implausible results compared to coincident AMSR-E and MHS observations because of excessive scattering. These unphysical T_B depressions are caused by inflated layer-derived IWC due to a priori Z_e–IWC relationships established for the ice particle models, as well as increased PSD-averaged extinction for some ice models. Recent work by Petty and Huang (2010) also highlights discrepancies between extinction and backscatter properties of spherical and complex aggregate ice models, so the results in this study confirm the inherent difficulty using spheres for combined active and passive microwave remote sensing applications. Nonspherical ice models from Hong (2007) and Liu (2008) possess more physically realistic combined microwave backscatter and extinction properties, and these models produce consistently better results when compared to multifrequency passive microwave observations of precipitation.

An ensemble approach using the Hong (2007) and Liu (2008) nonspherical ice models is adopted to highlight forward model uncertainties and errors due to the choice of ice particle model on a global scale. Overall, consistently negative model biases exist, but there is considerable variability in these results due to frequency, zenith angle, and precipitation type. The simulated T_B uncertainty due to the ice particle model is also shown to be as high as 9 K for the vertically polarized 89-GHz channel under heavier snowfall conditions, but this uncertainty is reduced to about 2 K in liquid precipitation regions and appears to be a strong function of IWP. Two other high-frequency nadir-viewing channels display lower uncertainties of about 4 (2) K for nadir 157 (89)-GHz simulated results under high-IWP conditions. The 157-GHz simulated brightness temperature uncertainties are also stratified by integrated CPR reflectivity above the freezing level (as a proxy for IWP), and precipitation-type dependencies are noted.

These results also indicate a one-size-fits-all precipitation categorization might not be the most optimal way to characterize forward model uncertainties and errors. It might be preferable to instead partition results into further subcategories based on a combination of latitude, precipitation type, and an integrated quantity indicative of columnar ice content (e.g., integrated CPR reflectivity above the freezing level). For instance, the stratiform category of precipitation displays distinctive trends between the various stratiform subcategories reported in this study. Variability in model error correlations and covariances between select microwave frequencies is evident owing to precipitation type and columnar ice amount, and the promise of improved all-weather data assimilation of microwave observations ultimately relies on better characterizing error correlation/covariance behavior under different precipitating conditions. Future efforts should be devoted to developing a larger combined active/passive microwave observational dataset to increase the sampling of all precipitation subcategories presented in this work. For instance, another stratiform precipitation category such as ''snowfall only'' could be developed with more observations to truly isolate errors due to scattering by frozen hydrometeors and decouple them from emission-based errors.

Future work will also be devoted to improve model components that may be the source of errors highlighted throughout this study. For instance, negative simulated 36- and 89-GHz biases observed under raining conditions are not directly related to scattering by frozen hydrometeors but, rather, to a possible combination of the following effects: 1) underestimation of columnar total water path, 2) liquid/ice partitioning near the freezing level (especially model-derived temperature errors exist), and 3) no explicit modeling of melting layer effects. Melting particles can significantly increase T_B emissions (e.g., Bauer et al. 1999), and the current methodology may accordingly suffer from no explicit treatment of the melting layer's enhanced emissive qualities. The 157-GHz channel, however, displays reduced biases compared to the lower frequencies under raining conditions, so this frequency seems more immune to emission-based bias sources because of its enhanced sensitivity to scattering by frozen particles aloft. Additionally, excessive scattering is evident in the 89-GHz oblique viewing angle simulations but not in the nadir 89- and 157-GHz results, so further work must be conducted to isolate this error source. In light of recent work by Matrosov and Battaglia (2009), multiple scattering versus attenuation effects in W-band snowfall observations must be studied more thoroughly, as the attenuation correction scheme employed in this study may contribute to excessive ice content that, in turn, can produce excessive scattering signals.

Finally, the large derived IWP uncertainties due to the ice model selected, combined with the simulated passive microwave results, indicate potential IWP retrieval implications. Even if the spherical models are disregarded, IWP uncertainties from the Z_e–IWC relationships still exceed 60% for the DDA ensemble in the higher IWP regions. These large IWP uncertainties, however, do not translate into particularly large simulated T_B uncertainties at a scattering sensitive frequency such as 157 GHz, and realistic T_B157 results are obtained using the DDA ensemble. These findings suggest that the accuracy of IWP retrievals using passive microwave observations in the 36–157-GHz range may suffer. It must be recognized, however, that IWP uncertainties are largely controlled by the Z_e–IWC relationships of the ice models used in this study, and many of the ice models are probably not representative of aggregate particles (from a mass-size perspective) that typically dominate snowfall, even though they adequately capture the radiative properties of frozen hydrometeors associated with precipitation. It must be noted that increased 157-GHz biases were associated with many ice models (e.g., certain columns and plates) for high IWP events, so the realism of these ice models may be questionable under such circumstances and must be tested further. If these questionable high-IWP nonspherical ice models were removed from the DDA ensemble, retrieved IWPs are reduced by ~10%–15%—a marked improvement, but the overall IWP uncertainty still exceeds about 45%. Continued work must still be undertaken to verify the physical mechanism responsible for the results presented in this study—especially isolating the influence of the derived PSD and PSD-averaged single-scatter properties on simulated T_B for each ice particle model—and to develop ice models more representative of aggregate-type particles.

Acknowledgments. The authors would like to acknowledge the *CloudSat* project and its Data Processing Center, as well as the National Snow and Ice Data Center and NOAA's Comprehensive Large Array Data Stewardship System, for products used in this study. Dr. Gang Hong is thanked for supplying microwave properties for some of the ice particle models used in this study. Dr. Guosheng Liu is gratefully acknowledged for making his database publicly available and easily accessible. Mr. Michael Hiley provided extensive and invaluable data processing assistance for this study. The authors would also like to thank three anonymous reviewers for their constructive comments. This work was partially funded by the Joint Center for Satellite Data Assimilation through NOAA Cooperative Agreement NA06NES4400002 and NASA Grant NNX07AE29G.

REFERENCES

Ashcroft, P., and F. Wentz, 2006: updated daily. AMSR-E/*Aqua* L2A global swath spatially resampled brightness temperatures V002, July 2006–January 2007. National Snow and Ice Data Center. [Available online at http://nsidc.org/data/ae_l2a.html.]

Austin, R., 2007: *CloudSat* ECMWF-AUX auxiliary data process description and interface control document, version 5.2. CloudSat Data Processing Center. [Available online at http://www.cloudsat.cira.colostate.edu/ICD/2B-CWC-RO/2B-CWC-RO_PD_5.1.pdf.]

Bauer, P., J. P. V. Poiares Baptista, and M. de Iulis, 1999: The effect of the melting layer on the microwave emission of clouds over the ocean. *J. Atmos. Sci.,* **56,** 852–867.

——, P. Lopez, A. Benedetti, D. Salmond, and E. Moreau, 2006a: Implementation of 1D+4D-Var assimilation of precipitation-affected microwave radiances at ECMWF. I: 1D-Var. *Quart. J. Roy. Meteor. Soc.,* **132,** 2277–2306.

——, ——, ——, ——, S. Saarinen, and M. Bonazzola, 2006b: Implementation of 1D+4D-Var assimilation of precipitation-affected microwave radiances in precipitation at ECMWF. II: 4D-Var. *Quart. J. Roy. Meteor. Soc.,* **132,** 2307–2332.

Bennartz, R., and G. W. Petty, 2001: The sensitivity of microwave remote sensing observations of precipitation to ice particle size distributions. *J. Appl. Meteor.,* **40,** 345–364.

——, and P. Bauer, 2003: Sensitivity of microwave radiances at 85–183 GHz to precipitating ice particles. *Radio Sci.,* **38,** 8075, doi:10.1029/2002RS002626.

Brown, P. R. A., and P. N. Francis, 1995: Improved measurements of the ice water content in cirrus using a total-water probe. *J. Atmos. Oceanic Technol.,* **12,** 410–414.

Chen, Y., F. Weng, Y. Han, and Q. Liu, 2008: Validation of the community radiative transfer model by using *CloudSat* data. *J. Geophys. Res.,* **113,** D00A03, doi:10.1029/2007JD009561.

DeBlonde, G., and S. J. English, 2001: Evaluation of the FASTEM-2 fast microwave oceanic surface emissivity model. *Tech. Proc. ITSC-XI,* Budapest, Hungary, WMO, 67–78.

Draine, B. T., and P. J. Flatau, 1994: Discrete-dipole approximation for scattering calculations. *J. Opt. Soc. Amer.,* **11A,** 1491–1499.

Ellis, T. D., T. L'Ecuyer, J. M. Haynes, and G. L. Stephens, 2009: How often does it rain over the global oceans? The perspective from *CloudSat*. *Geophys. Res. Lett.,* **36,** L03815, doi:10.1029/2008GL036728.

English, S. J., R. J. Renshaw, P. C. Dibben, A. J. Smith, P. J. Rayer, C. Poulsen, F. W. Saunders, and J. R. Eyre, 2000: A comparison of the impact of TOVS and ATOVS satellite sounding data on the accuracy of numerical weather forecasts. *Quart. J. Roy. Meteor. Soc.,* **126,** 2911–2931.

Errico, R. M., P. Bauer, and J. Mahfouf, 2007a: Issues regarding the assimilation of cloud and precipitation data. *J. Atmos. Sci.,* **64,** 3785–3798.

——, G. Ohring, P. Bauer, B. Ferrier, J. Mahfouf, J. Turk, and F. Weng, 2007b: Assimilation of satellite cloud and precipitation observations in numerical weather prediction models: Introduction to the JAS special collection. *J. Atmos. Sci.,* **64,** 3737–3741.

Evans, K. F., 2007: SHDOMPPDA: A radiative transfer model for cloudy sky data assimilation. *J. Atmos. Sci.,* **64,** 3854–3864.

Field, P. R., R. J. Hogan, P. R. A. Brown, A. J. Illingworth, T. W. Choularton, and R. J. Cotton, 2005: Parametrization of ice-particle size distributions for mid-latitude stratiform cloud. *Quart. J. Roy. Meteor.Soc.,* **131,** 1997–2017, doi:10.1256/qj.04.134.

——, A. Heymsfield, and A. Bansemer, 2007: Snow size distribution parameterization for midlatitude and tropical ice clouds. *J. Atmos. Sci.,* **64,** 4346–4365.

Greenwald, T., R. Bennartz, C. O'Dell, and A. Heidinger, 2005: Fast computation of microwave radiances for data assimilation using the ''successive order of scattering'' method. *J. Appl. Meteor.,* **44,** 960–966.

Han, Y., P. van Delst, Q. Liu, F. Weng, B. Yan, R. Treadon, and J. Derber, 2006: Community Radiative Transfer Model (CRTM): Version 1. NOAA Tech. Rep. 122, 33 pp.

Heidinger, A. K., C. O'Dell, R. Bennartz, and T. Greenwald, 2006: The successive-order-of-interaction radiative transfer model. Part I: Model development. *J. Appl. Meteor. Climatol.,* **45,** 1388–1402.

Hilburn, K. A., and F. J. Wentz, 2008: Intercalibrated passive microwave rain products from the unified microwave ocean retrieval algorithm (UMORA). *J. Appl. Meteor. Climatol.,* **47,** 778–794.

Hong, G., 2007: Parameterization of scattering and absorption properties of nonspherical ice crystals at microwave frequencies. *J. Geophys. Res.,* **112,** D11208, doi:10.1029/2006JD008364.

Kawanishi, T., and Coauthors, 2003: The Advanced Microwave Scanning Radiometer for the Earth Observing System (AMSR-E): NASDA's contribution to the EOS for global energy and water cycle studies. *IEEE Trans. Geosci. Remote Sens.,* **41,** 184–194, doi:10.1109/TGRS.2002.808331.

Kelly, G. A., P. Bauer, A. J. Geer, P. Lopez, and J. Thépaut, 2008: Impact of SSM/I observations related to moisture, clouds, and precipitation on global NWP forecast skill. *Mon. Wea. Rev.,* **136,** 2713–2726.

Kim, M.-J., M. S. Kulie, C. O'Dell, and R. Bennartz, 2007: Scattering of ice particles at microwave frequencies: A physically based parameterization. *J. Appl. Meteor. Climatol.,* **46,** 615–633.

Kongoli, C., P. Pellegrino, R. Ferraro, N. Grody, and H. Meng, 2003: A new snowfall detection algorithm over land using measurements from the Advanced Microwave Sounding Unit (AMSU). *Geophys. Res. Lett.,* **30,** 1756, doi:10.1029/2003GL017177.

Kulie, M. S., and R. Bennartz, 2009: Utilizing spaceborne radars to retrieve dry snowfall. *J. Appl. Meteor.,* **48,** 2564–2580.

L'Ecuyer, T. S., and G. L. Stephens, 2002: An estimation-based precipitation retrieval algorithm for attenuating radars. *J. Appl. Meteor.,* **41,** 272–285.

Liebe, H. J., G. A. Hufford, and T. Manabe, 1991: A model for the complex permittivity of water at frequencies below 1 THz. *Int. J. Infrared Millimeter Waves,* **12,** 659–675.

Liu, C., and E. J. Zipser, 2009: ''Warm rain'' in the tropics: Seasonal and regional distributions based on 9 yr of TRMM data. *J. Climate,* **22,** 767–779.

Liu, G., 2008: A database of microwave single-scattering properties for nonspherical ice particles. *Bull. Amer. Meteor. Soc.,* **89,** 1563–1570.

Liu, Q., and F. Weng, 2006: Advanced doubling–adding method for radiative transfer in planetary atmospheres. *J. Atmos. Sci.,* **63,** 3459–3465.

Locatelli, J. D., and P. V. Hobbs, 1974: Fall speeds and masses of solid precipitation particles. *J. Geophys. Res.,* **79,** 2185–2197.

Mahfouf, J. F., P. Bauer, and V. Marécal, 2005: The assimilation of SSM/I and TMI rainfall rates in the ECMWF 4D-Var system. *Quart. J. Roy. Meteor. Soc.,* **131,** 437–458, doi:10.1256/qj.04.17.

Matrosov, S. Y., and A. Battaglia, 2009: Influence of multiple scattering on *CloudSat* measurements in snow: A model study. *Geophys. Res. Lett.,* **36,** L12806, doi:10.1029/2009GL038704.

McCollum, J., and R. Ferraro, 2003: Next generation of NOAA/NESDIS TMI, SSM/I, and AMSR-E microwave land rainfall algorithms. *J. Geophys. Res.,* **108,** 8382, doi:10.1029/2001JD001512.

Mitchell, D. L., 1996: Use of mass- and area-dimensional power laws for determining precipitation particle terminal velocities. *J. Atmos. Sci.,* **53,** 1710–1723.

O'Dell, C. W., A. K. Heidinger, T. Greenwald, P. Bauer, and R. Bennartz, 2006: The successive-order-of-interaction radiative transfer model. Part II: Model performance and applications. *J. Appl. Meteor. Climatol.,* **45,** 1403–1413.

——, F. J. Wentz, and R. Bennartz, 2008: Cloud liquid water path from satellite-based passive microwave observations: A new climatology over the global oceans. *J. Climate,* **21,** 1721–1739.

Petty, G. W., 1994: Physical retrievals of over-ocean rain rate from multichannel microwave imagery. Part I: Theoretical characteristics of normalized polarization and scattering indexes. *Meteor. Atmos. Phys.,* **54,** 79–99.

——, and W. Huang, 2010: Microwave backscatter and extinction by soft ice spheres and complex snow aggregates. *J. Atmos. Sci.,* **67,** 769–787.

Rosenkranz, P. W., 1998: Water vapor microwave continuum absorption: A comparison of measurements and models. *Radio Sci.,* **33,** 919–928.

Sassen, K. S., S. Matrosov, and J. Campbell, 2007: *CloudSat* spaceborne 94 GHz radar bright bands in the melting layer: An attenuation-driven upside-down lidar analog. *Geophys. Res. Lett.,* **34,** L16818, doi:10.1029/2007GL030291.

Spencer, R. W., H. M. Goodman, and R. E. Hood, 1989: Precipitation retrieval over land and ocean with the SSM/I: Identification and characteristics of the scattering signal. *J. Atmos. Oceanic Technol.,* **6,** 254–273.

Stephens, G. L., and Coauthors, 2002: The *CloudSat* mission and the A-Train: A new dimension of space-based observations of clouds and precipitation. *Bull. Amer. Meteor. Soc.,* **83,** 1771–1790.

Surussavadee, C., and D. H. Staelin, 2006: Comparison of AMSU millimeter-wave satellite observations, MM5/TBSCAT predicted radiances, and electromagnetic models for hydrometeors. *IEEE Trans. Geosci. Remote Sens.,* **44,** 2667–2678, doi:10.1109/TGRS.2006.873275.

Tanelli, S., S. L. Durden, E. Im, K. S. Pak, D. G. Reinke, P. Partain, J. M. Haynes, and R. T. Marchand, 2008: *CloudSat*'s cloud profiling radar after two years in orbit: Performance, calibration, and processing. *IEEE Trans. Geosci. Remote Sens.,* **46,** 3560–3573.

Thompson, G., P. R. Field, R. M. Rasmussen, and W. D. Hall, 2008: Explicit forecasts of winter precipitation using an improved bulk microphysics scheme. Part II: Implementation of a new snow parameterization. *Mon. Wea. Rev.,* **136,** 5095–5115.

Weng, F., N. C. Grody, R. Ferraro, A. Basist, and D. Forsyth, 1997: Cloud liquid water climatology from the Special Sensor Microwave/Imager. *J. Climate,* **10,** 1086–1098.

——, T. Zhu, and B. Yan, 2007: Satellite data assimilation in numerical weather prediction models. Part II: Uses of rain-affected radiances from microwave observations for hurricane vortex analysis. *J. Atmos. Sci.,* **64,** 3910–3925.

Wentz, F., and T. Meissner, 2004: updated daily. AMSR-E/*Aqua* L2B global swath ocean products derived from Wentz algorithm V002, July 2006–January 2007. National Snow and Ice Data Center. [Available online at http://nsidc.org/data/ae_ocean.html.]

Zhao, L. M., and F. Z. Weng, 2002: Retrieval of ice cloud parameters using the Advanced Microwave Sounding Unit. *J. Appl. Meteor.,* **41,** 384–395.